



POLITECNICO
MILANO 1863

SCUOLA DI INGEGNERIA INDUSTRIALE
E DELL'INFORMAZIONE

SPACECRAFT ATTITUDE DYNAMICS

ACADEMIC YEAR 2024/2025

Project group n. 34
PROJECT N. 238

Prof Franco Bernelli Zazzera

Team Members

Person Code	Surname	Name	Bachelor
11072547	Azevedo Da Silva	Esteban	ISAE-ENSMA Aerospace master
10797598	Domenichelli	Eleonora	Politecnico di Milano Aerospace Engineering
10766052	Donati	Filippo	Politecnico di Milano Aerospace Engineering
11021048	Pantoja Gavidia	Maria Paulina	Instituto Politécnico Nacional Aeronautical Engineering

LAUREA MAGISTRALE
SPACE ENGINEERING

Project Specifications

Platform	Assigned specification	Modifications (if any)	Motivation for modification
Attitude parameters	Euler Angles		
Mandatory sensor	Sun sensors	Magnetometer	To get full attitude determination
Actuators	Control Moment gyroscope		

Contents

Project Specifications	i
1 Introduction	1
1.1 Satellite Selection	2
1.2 Mission Description and Pointing Requirements	2
1.3 Orbit Specifications	3
2 Environment Model	3
2.1 Dynamics	4
2.2 Kinematics	4
2.2.1 Attitude Kinematics	4
2.2.2 Orbital Kinematics	5
2.3 Environment	5
2.3.1 Sun Direction and Shadow	5
2.3.2 Magnetic field	5
2.3.3 Disturbances	6
2.3.3.1 Gravity Gradient Torque	7
2.3.3.2 Magnetic Torque	7
2.3.3.3 Atmospheric Drag	7
2.3.3.4 Solar Radiation Pressure Torque	8

3	ADCS Architecture	8
3.1	Hardware Architecture	8
3.1.1	Sensors	8
3.1.1.1	Sun Sensors	8
3.1.1.2	Magnetometer	9
3.1.2	Actuators	10
3.1.2.1	Control Moment Gyroscopes	10
3.2	Software Architecture	11
3.2.1	Reference	11
3.2.2	Navigation	11
3.2.2.1	QUEST Implementation	12
3.2.2.2	State Observer	13
3.2.3	Control	14
3.2.3.1	Sun Pointing Law	14
3.2.3.2	Re-Pointing / Slew Maneuver Law	15
3.2.3.3	Detumbling	15
4	Results	16
4.1	Control Results	16
4.2	Monte-Carlo test campaign	18
4.2.1	Re-Pointing Monte-Carlo	18
4.2.2	De-tumbling Monte-Carlo	18
4.3	Eclipse behavior	19
5	Conclusions	20
	Bibliography	21

1 | Introduction

This report presents the development and simulation of a 6U CubeSat's Attitude Determination and Control System (ADCS), designed for a Sun-pointing mission as part of the "Spacecraft Attitude Dynamics" course during the fall semester of 2024-2025. The CubeSat's mission is to stabilize its orientation and accurately point toward the Sun, which was achieved through the mandatory use of a Sun sensor as the primary measurement device. The rotational motion was modeled using Euler angles, and attitude determination was refined with the support of a tri-axial magnetometer for enhanced accuracy, while Control Moment Gyroscopes (CMGs) served as actuators to achieve precise orientation control.

To implement the ADCS, a model was developed in MATLAB Simulink® to represent the interaction between the real-world dynamics and the On-Board Computer (OBC), as shown in Figure 1.1. This approach allowed the simulation to closely approximate the behavior of a real mission by modeling two main environments: the real-world dynamics and the control system onboard the satellite.

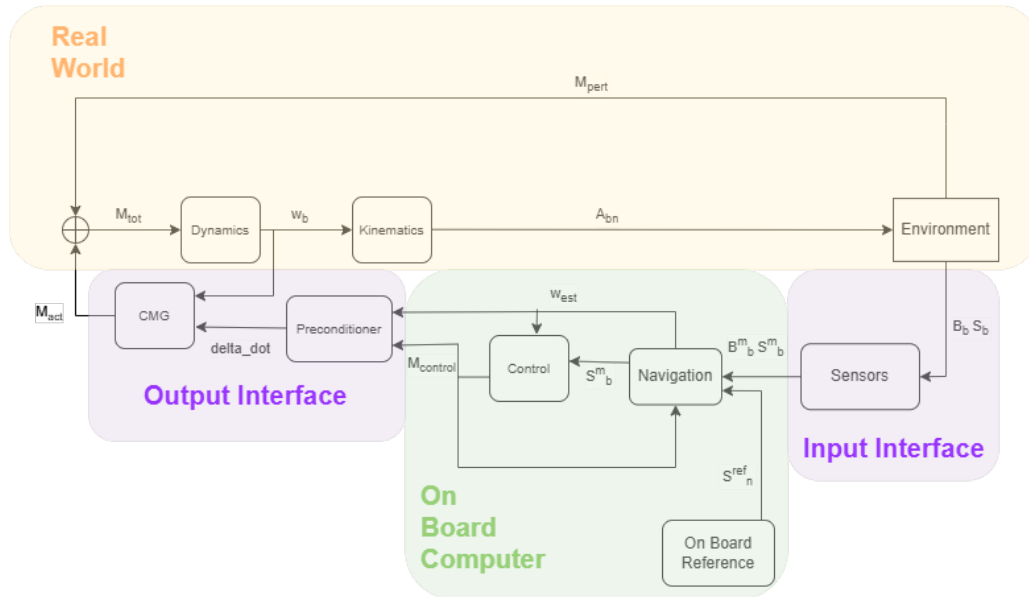


Figure 1.1: Model Scheme

The real-world environment includes the Dynamics Kinematics Environment (DKE), which simulates the dynamics and kinematics of the CubeSat under the influence of external disturbances and applied control torques. This environment is interfaced with a hardware model that represents the in-

teraction of the satellite with its physical surroundings through sensors and actuators. The On-Board Computer (OBC) acts as the central processing hub of the control system, receiving data from the hardware model and processes this information using attitude determination and control algorithms to adapt it into actionable commands for the actuators, ensuring the CubeSat achieves the desired attitude behavior.

1.1. Satellite Selection

The 6U CubeSat was designed using the NanoAvionics M6P COTS [1] casing with overall dimensions of $119 \times 226 \times 366$ mm and a total mass assumed to be homogeneously distributed at 7 kg [2]. In addition, two solar panels were incorporated into the design with dimensions of $110 \times 210 \times 15$ mm copying typical configurations for power systems in similar satellites as covering approximately 95% of the CubeSat's lateral surface [3]. Table 1.1 represents the dimensions considered.

Table 1.1: Cubesat properties

	Mass (kg)	Dimensions (mm)
Body	7	$119 \times 226 \times 366$
Panels (x2)	0.3175	$110 \times 210 \times 15$

A CAD model was created in SolidWorks, as shown in Figure 1.2, incorporating the characteristics described above, which resulting configuration defines a total mass (M_{tot}) of 7.635 kg and places the center of gravity (r_{GC}) at $[0, 0, -0.8776]$ mm. From this mass distribution, the moment of inertia was determined and expressed as:

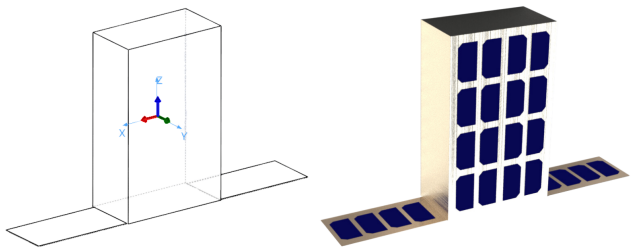
$$I = \begin{bmatrix} 0.04327 & 0 & 0 \\ 0 & 0.095068 & 0 \\ 0 & 0 & 0.120327 \end{bmatrix} \text{ kg/m}^2$$


Figure 1.2: Cubesat CAD model

For the purpose of this simulation, the CubeSat is assumed to behave as a completely rigid body, with no deformations, vibrations, or geometric irregularities. Only rigid-body rotational attitude dynamics are considered, excluding the effects of structural flexibility and all the components are modeled as rigid bodies, and internal energy dissipation due to elastic deformations or energy storage in flexible structures is omitted.

1.2. Mission Description and Pointing Requirements

The overall goal of this mission is to observe the Sun using a new camera system mounted on the $+\hat{z}_b$ face of the satellite, in order to study its properties. This decision was made because the satellite

is required to have a Sun sensor, providing reliable measurements of the Sun's direction. However, during eclipse periods, when no information on the Sun's position is available, the satellite will not be able to actively control its orientation. As a result, the control law will involve active pointing along the \hat{z}_b axis while maintaining the spacecraft's rotation around the same axis (the major inertial axis) at a constant rate ω_s , in order to take advantage of gyroscopic stability during eclipses.

Thus, the pointing requirement during the Sun phase is set to a maximum allowable error of 1° to ensure accurate Sun observation. During eclipses, while pointing at the Sun becomes irrelevant, the pointing requirement is maintained to ensure rapid resumption of operations after the eclipse phase ends. To this end, the maximum pointing error is set to 15° to rely on passive stability during eclipse periods.

1.3. Orbit Specifications

To achieve the mission objectives, a Sun-synchronous orbit with a dawn-dusk configuration was selected to maximize the satellite's exposure to sunlight. This dawn-dusk orbit, characterized by a RAAN of -90° at the spring equinox, was further defined with an eccentricity of 0 and an inclination (i) of 98.9897° , as detailed in Table 3.1. Additionally, to optimize operational efficiency and minimize the number of required ground stations, a repetitive orbit with $k=14$ was chosen, which determined the semi-major axis (a) to be 7258,69 km.

Table 1.2: Orbital parameters

a [km]	e [-]	i [deg]	Ω [deg]
7258.69	0	98.9897	-90

2 | Environment Model

To perform an accurate analysis of the overall behavior of the ADCS Algorithms, a model called Dynamics Kinematics and Environment (DKE) was implemented providing a structured approach to represent factors such as physical conditions and disturbances. By incorporating these environmental factors, the ADCS can be tested and refined under realistic conditions, ensuring reliable performance during the mission.

2.1. Dynamics

The rotational dynamics of the CubeSat are described by Euler's equations of motion, as shown in Equation 2.1, where the external moment M represents the net torque applied to the satellite, including control inputs and environmental disturbances. To simplify the model and focus on primary rotational effects, the inertia matrix I is assumed to be diagonal. This assumption eliminates the products of inertia and allows the equations to be expressed in their simplified form, as shown in Equation 2.2.

$$\mathbf{I}\dot{\boldsymbol{\omega}} + \boldsymbol{\omega} \times (\mathbf{I}\boldsymbol{\omega}) = \mathbf{M} \quad (2.1)$$

For a diagonal inertia matrix $I = \text{diag}(I_x, I_y, I_z)$, the individual components of Euler's equations are:

$$\begin{cases} I_x \dot{\omega}_x = M_x - (I_y - I_z) \omega_y \omega_z \\ I_y \dot{\omega}_y = M_y - (I_z - I_x) \omega_z \omega_x \\ I_z \dot{\omega}_z = M_z - (I_x - I_y) \omega_x \omega_y \end{cases} \quad (2.2)$$

2.2. Kinematics

2.2.1. Attitude Kinematics

The rotational dynamics of the CubeSat was modeled using the Euler angles formulation to represent the orientation as a sequence of three rotations about specific axes. This approach, while effective, introduces singularities at specific angular configurations, particularly when the pitch angle nears $\pm 90^\circ$, leading to discontinuities in the kinematic equations. To overcome this limitation, the system employed two distinct Euler angle sequences-313 (shown in Equation 2.3a) and 312 (shown in Equation 2.3b) - with a switching logic implemented to transition between them as singularities were approached.

$$\begin{aligned} \dot{\phi} &= \frac{-(\omega_z \cos \psi - \omega_x \sin \psi)}{\sin \theta}, & \dot{\phi} &= \frac{(\omega_z \cos \psi - \omega_x \sin \psi)}{\cos \theta}, \\ \dot{\theta} &= \omega_x \cos \psi - \omega_y \sin \psi, & \dot{\theta} &= \omega_x \cos \psi + \omega_y \sin \psi, \\ \dot{\psi} &= \omega_z - (\omega_x \sin \psi + \omega_y \cos \psi) \frac{\cos \theta}{\sin \theta}, & \dot{\psi} &= \omega_y - (\omega_z \cos \psi - \omega_x \sin \psi) \frac{\sin \theta}{\cos \theta} \end{aligned} \quad \begin{matrix} (2.3a) \\ (2.3b) \end{matrix}$$

Once the Euler angles are propagated, they serve as the basis for calculating the rotation matrix A_{bn} , which transforms vectors between the inertial (n-frame) and body-fixed (b-frame) reference frames. The specific derivation of A_{bn} depends on the chosen sequence; it is calculated using the formulations expressed in Equation 2.4a for the 313 representation and Equation 2.4b for the 312 representation.

$$A_{bn} = R_3(\psi)R_2(\theta)R_1(\phi) \quad (2.4a)$$

$$A_{bn} = R_3(\psi)R_2(\phi)R_1(\theta) \quad (2.4b)$$

2.2.2. Orbital Kinematics

The orbital kinematics of the CubeSat were simulated using Kepler's equations, modeling its motion under the influence of Earth's gravitational field based on the integration of the true anomaly 2.5. The dynamics were simplified by focusing on the two-body problem and neglecting perturbations such as third-body accelerations which allowed the CubeSat's position in the inertial frame (\vec{r}_N) to be expressed as outlined in Equation 2.6.

$$\dot{\theta} = \sqrt{\frac{\mu(1+e) \cdot \cos \theta}{a^3(1-e^2)^{3/2}}} \quad (2.5) \quad \vec{r}_N = \begin{bmatrix} x \\ y \\ z \end{bmatrix} = r \begin{bmatrix} \cos \theta \\ \sin \theta \cos i \\ \sin \theta \sin i \end{bmatrix} \quad (2.6)$$

However, the effects of Earth's oblateness, specifically the J_2 perturbation, were partially considered to account for the precession of the RAAN as given in Equation 2.7, which was included to maintain the Sun-synchronous nature of the orbit

$$i = \arccos \left(\frac{-2 \dot{\Omega} a^{7/2} (1-e^2)^2}{3 J_2 R_E^2 \sqrt{\mu}} \right) \quad (2.7)$$

2.3. Environment

2.3.1. Sun Direction and Shadow

To evaluate the Sun's direction and the shadowing effects caused by Earth, a set of simplifying assumptions was adopted.

Initially, it was assumed that the Sun's distance from the Earth ($S_{\oplus\odot}$) is significantly larger than the CubeSat's distance from the Earth ($S_{\oplus sc}$). This assumption allows the Sun's direction vector relative to the spacecraft to be approximated as identical to its direction relative to Earth.

Furthermore, Earth's orbit around the Sun was considered circular, with a period of one year, simplifying the calculations of the Sun's apparent position.

To assess whether the CubeSat is in sunlight or shadow, a cylindrical shadow model was implemented. This model evaluates the geometry of the Sun-Earth-CubeSat alignment to determine whether Earth blocks sunlight from reaching the spacecraft, and when the CubeSat is in a condition to be in shadow is described by Equation 2.8 whose derivation is trivial [4].

$$\mathbf{r} \cdot \mathbf{e}_{\oplus\odot} < -\sqrt{r^2 - R_{\oplus}^2} \quad (2.8)$$

2.3.2. Magnetic field

The Earth's magnetic field was modeled using a simplified version of the International Geomagnetic Reference Field (IGRF), truncated to the first term, commonly referred to as the dipole model, shown

in Equation 2.9. Although this approach reduces accuracy compared to a full IGRF expansion, it is sufficient given the absence of onboard magnetic control systems.

$$\vec{B} = H_0 R^3 \left(\frac{3(\vec{m} \cdot \hat{r})\hat{r} - \vec{m}}{\|\vec{r}\|^3} \right) \quad (2.9)$$

To ensure computational efficiency, the model assumes a constant dipole moment aligned with Earth's rotational axis. Under this assumption, the magnetic field vector in the body-fixed frame can be calculated directly using Equation 2.10.

$$\vec{B}_b = A_{bn} \cdot \vec{B}_n \quad (2.10)$$

Despite its simplified representation, this model offers flexibility for future applications by incorporating additional harmonic terms from the IGRF series to achieve greater precision if required for more demanding missions.

2.3.3. Disturbances

The CubeSat's motion and orientation are affected by various environmental disturbances, which manifest as external torques influencing its dynamics and stability, among these, the four primary disturbances—Gravity Gradient Torque, Atmospheric drag, Solar Radiation Pressure, and Magnetic Torque—play a significant role. Nevertheless, as shown in Figure 2.1, due to the CubeSat's altitude and dimensions, Gravity Gradient Torque and Magnetic Torque have the greatest impact on its behavior. Consequently, these two disturbances have been prioritized and will be the primary focus of this study.

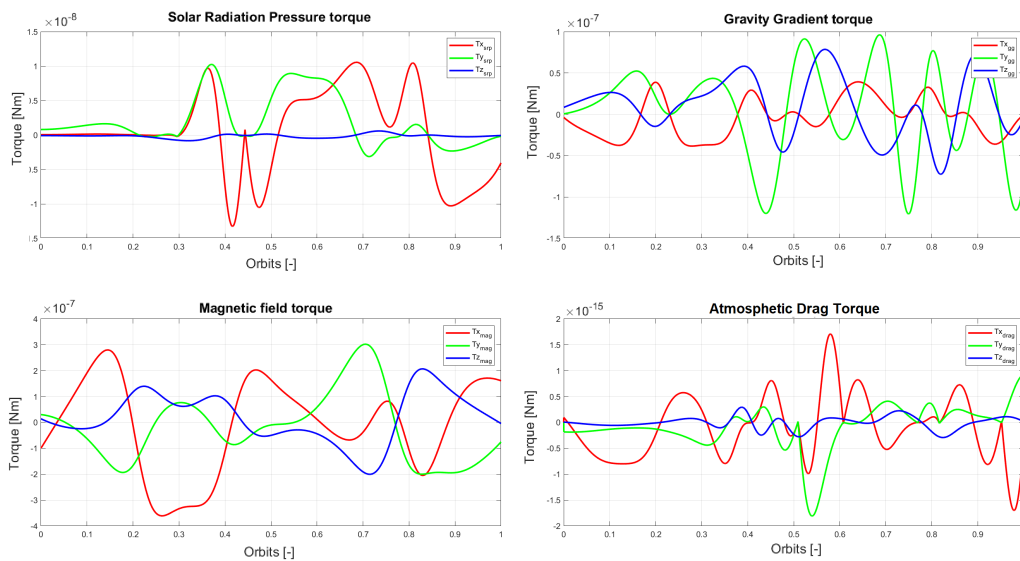


Figure 2.1: Perturbation Comparison

2.3.3.1. Gravity Gradient Torque

The gravity gradient torque is given by Equation 2.11 as a consequence of the interaction between the Earth's gravitational field and the distribution of mass of the CubeSat caused by the variation in gravitational force across the satellite's structure, resulting in a restoring moment that aligns the satellite's principal axis of inertia with the local vertical direction, this effect is particularly pronounced in zones as the studied orbit.

$$T_{gg} = \frac{3\mu}{\|\vec{r}\|^3} (\mathbf{I} \cdot \mathbf{c}) \times \mathbf{c} \rightarrow \begin{bmatrix} c_1 \\ c_2 \\ c_3 \end{bmatrix} = A_{BL} \begin{bmatrix} 1 \\ 0 \\ 0 \end{bmatrix} \quad (2.11)$$

2.3.3.2. Magnetic Torque

As expressed in Equation 2.12, the magnetic torque results from the interaction between Earth's magnetic field and the CubeSat's residual magnetic dipole moment, estimated, following the procedure listed in [5], as $[0.27; 0.53; 0.78] * 0.01 Am^2$. This interaction generates a torque that can significantly influence the satellite's attitude, particularly in the studied orbit, where the magnetic field remains relatively strong.

$$T_{mag} = J_B \times B_b \quad (2.12)$$

This disturbance is highly dynamic due to the variations in the Earth's magnetic field along the CubeSat's orbit.

2.3.3.3. Atmospheric Drag

Atmospheric drag, as described in Equation 2.13, arises from the interaction between residual atmospheric particles and the CubeSat's surface.

$$T_{aero} = -\frac{1}{2} \rho C_D v_{rel}^2 \left(\sum_{i=1}^n \vec{r}_i \wedge \frac{\vec{v}_{rel}^b}{\|\vec{v}_{rel}^b\|} \right) + \sum_{i=1}^n \left(\vec{N}_{bi} \cdot \frac{\vec{v}_{rel}^b}{\|\vec{v}_{rel}^b\|} \right) \vec{A}_i \quad (2.13)$$

While the drag force is amplified by the CubeSat's relative velocity, it also depends on factors such as the satellite's shape, orientation, with a drag coefficient (C_d) of 2.4 (approximated using Athena Vortex Lattice) and the atmospheric density (From equation 2.14 and ISA measurements). However, due to the extremely low atmospheric density at the CubeSat's orbital altitude, this perturbation becomes negligible compared to other disturbances.

$$\rho = \rho_0 \exp -\frac{h - h_0}{H} \quad (2.14)$$

2.3.3.4. Solar Radiation Pressure Torque

Solar radiation pressure (SRP) torque, as detailed in Equation 2.15, is caused by the momentum transfer of solar photons impacting the CubeSat's surface, which creates a net torque from unevenly distributed forces across the structure. Although the force's magnitude is relatively small, it can induce significant torques based on the CubeSat's surface properties, geometry, and its orientation relative to the Sun. Each surface independently contributes to the total torque, and shadowing effects are accounted for to adjust the effective solar force as the CubeSat enters partial or full shadow regions. The reflection coefficients ρ_s and ρ_d were established based on the materials of the M6P.

$$T_{SRP} = \sum_{i=1}^n \left(-PA_i(\vec{S}_b \cdot \vec{N}_{bi}) \left[(1 - \rho_s)\vec{S}_b + (2\rho_s(\vec{S}_b \cdot \vec{N}_{bi}) + \frac{2}{3}\rho_d)\vec{N}_{bi} \right] \right) \times \vec{r}_i \quad (2.15)$$

Despite the SRP torque being relatively minor compared to other disturbances due its dimensions, its cumulative effects over time can significantly alter the CubeSat's attitude.

3 | ADCS Architecture

3.1. Hardware Architecture

The Hardware Architecture of the CubeSat show in Figure 3.1 covers the modeling and integration of its primary components, specifically the actuators and sensors, within a unified simulation framework. This subsystem design ensures a realistic representation of the interactions between the CubeSat's physical environment and onboard computational systems as provide the necessary feedback and control inputs to achieve the mission's orientation requirements.

3.1.1. Sensors

3.1.1.1. Sun Sensors

The CubeSat employs a set of five Sun sensors inspired by the SolarMEMS nanoSSOC-D60 model [6], which are critical for determining the satellite's orientation relative to the Sun. These sensors, mounted orthogonally on the CubeSat's faces, are designed to provide reliable and precise measurements of the Sun's position within their field of view (FOV), as detailed in Table 3.1 with their main properties.

The Sun sensor model integrates various error sources to simulate realistic operational conditions. It accounts for misalignment errors during installation, finite sensor precision, inherent accuracy limits, and the discretization effects of the 10-bit ADC. These factors enable a comprehensive evaluation

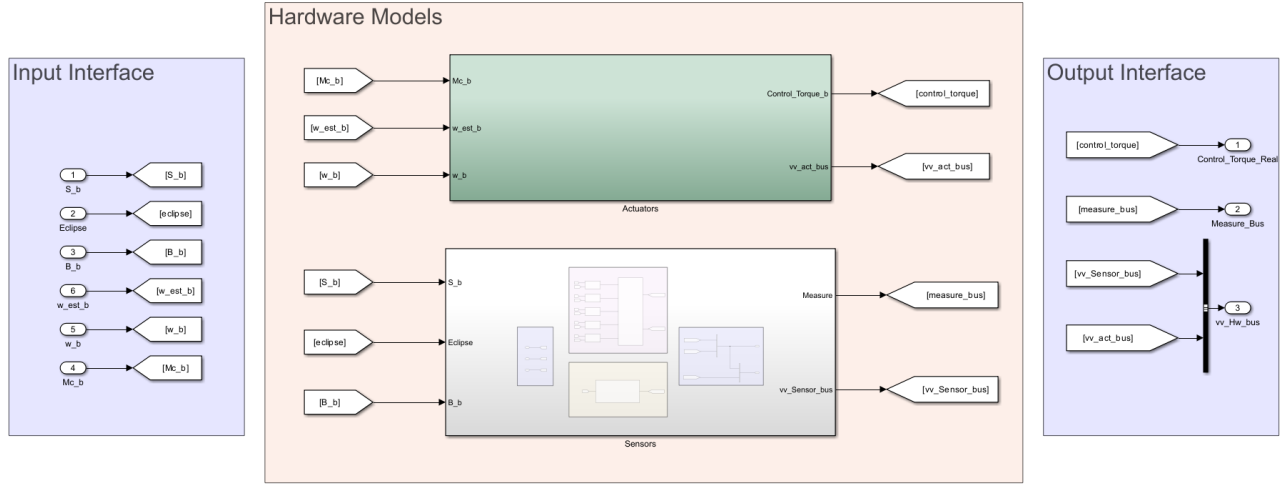


Figure 3.1: Hardware Model

Table 3.1: Sun sensor properties

Model	Sensor Type	FOV	Accuracy	Precision	ADC
nanoSSOC-D60	Orthogonal	60°	0.5°	0.1°	10 bits

of the sensors' performance in the simulation environment, ensuring that the input to the attitude determination system accurately reflects realistic constraints.

Certain factors, such as errors arising from electrical communication with the onboard computer (OBC) and inaccuracies in calibration functions, were excluded from the model. These omissions are justified by their minimal impact within the mission's scope. By focusing on the most significant error sources, the model achieves a balance between computational efficiency and a realistic representation of the sensors' performance.

3.1.1.2. Magnetometer

To complement the Sun Sensors and provide independent directional measurements, a three-axis MEMS magnetometer was included in the CubeSat's sensor suite. This additional sensor enhances the accuracy and redundancy of the attitude determination system by measuring the Earth's magnetic field. The magnetometer model is inspired by the Honeywell HMC5843, with dimensions of $4 \times 4 \times 1.3$ mm.

In the simulation, the magnetometer was modeled with key characteristics that reflect the performance of the actual sensor by including a measurement range between -4 and +4 Gauss, a resolution of 7 mGauss, and a sampling frequency of 10 Hz. To accurately replicate operational conditions, various error sources were integrated, such as misalignment, cross-axis sensitivity, and noise variance. The signal-to-noise ratio provided in the datasheet of the HMC5843 was used to estimate the maximum noise variance included in the model.

The magnetometer serves as a critical component of the sensor suite, providing three-dimensional

measurements of the Earth's magnetic field which are essential for complementing the Sun Sensor data, particularly when determining the CubeSat's orientation in eclipsed regions where sunlight is not available.

3.1.2. Actuators

3.1.2.1. Control Moment Gyroscopes

The CubeSat's attitude control system is equipped with a set of four single-gimbal Control Moment Gyroscopes (CMGs) arranged in a pyramidal configuration which provides full three-axis control while incorporating redundancy to ensure operational reliability. The CMGs are based on the design proposed by Baker [7] and are characterized by a nominal skew angle (β) of 54.74° , with each unit providing a fixed angular momentum of 1.4 mN·ms.

The torque generated by the CMGs is determined using the relationship between the gimbal angles, angular velocities, and the resultant angular momentum, as expressed in Equation 3.1

$$\dot{h}_{CMG} = \dot{A}h_r = B\dot{\delta} = h_r \underbrace{\begin{bmatrix} -\cos\beta\cos\delta_1 & \sin\delta_2 & \cos\beta\cos\delta_3 & -\sin\delta_4 \\ -\sin\delta_1 & -\cos\beta\sin\delta_2 & \sin\delta_3 & \cos\beta\cos\delta_4 \\ \sin\beta\cos\delta_1 & \sin\beta\sin\delta_2 & \sin\beta\cos\delta_3 & \sin\beta\sin\delta_4 \end{bmatrix}}_B \underbrace{\begin{bmatrix} \dot{\delta}_1 \\ \dot{\delta}_2 \\ \dot{\delta}_3 \\ \dot{\delta}_4 \end{bmatrix}}_{\dot{\delta}} \quad (3.1)$$

The hardware implementation accounts for several practical constraints. The maximum gimbal velocity is limited to -10rad/s to $+10\text{rad/s}$, ensuring that the gimbal motors operate within safe mechanical limits. Furthermore, the angular position of each gimbal is quantized with a resolution of 0.0879° , reflecting the precision of the hardware encoders. Additionally, the PWM signal that drives the gimbal movement is modeled with 16-bit quantization, balancing the need for control accuracy and computational efficiency.

Despite the advantages of CMGs, their operation is subject to the phenomenon of saturation, a limitation inherent to this type of actuator. Saturation occurs when the gimbals can no longer produce the required torque due to the accumulation of angular momentum; this issue is particularly significant in CMGs as they do not generate external torque, meaning their momentum builds up over time. While the current model does not include additional actuators, such as magnetic torquers, these devices are commonly used in real-world scenarios to desaturate the system and maintain control authority. The inclusion of magnetic actuators in future iterations is highly recommended to address this challenge effectively.

3.2. Software Architecture

The Software Model of the CubeSat, as shown in Figure 3.2, represents the computational core responsible for processing sensor data, determining the satellite's state, and generating control commands to meet mission requirements. This model integrates key functional blocks, including navigation, guidance, and control (GNC), along with support subsystems for reference generation and operational mode management.

All these processes within the onboard computer (OBC) are discrete and operate at a fixed frequency of 25 Hz ensuring synchronization and consistency across the computational framework. By simulating the onboard algorithms within this framework, the Software Model ensures accurate and efficient data flow between the sensor inputs, state estimation processes, and actuator outputs, achieving precise attitude control and navigation, bridging the gap between the CubeSat's hardware components and its dynamic operating environment.

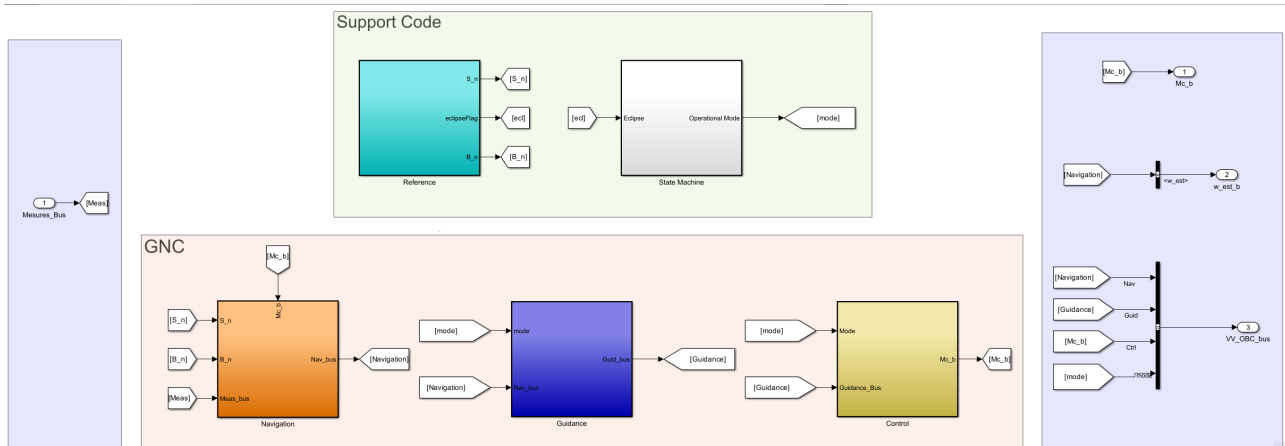


Figure 3.2: Software Model

3.2.1. Reference

This subsystem provides precise directional information necessary for attitude estimation using the QUEST algorithm, that requires at least two vectors defined both in the body frame and the reference frame. To meet this requirement, the Reference subsystem incorporates mathematical models of the Sun's position and Earth's magnetic field. In this implementation, the models align exactly with those used in the Environment subsystem, ensuring consistency and accuracy, and calculate the expected positions and orientations of the Sun and the magnetic field relative to the CubeSat, enabling the attitude determination system to compare measured directions with the calculated reference directions. While this specific implementation employs detailed environmental models, in broader applications, the Reference subsystem could employ simplified descriptions to reduce computational demands while maintaining sufficient accuracy for attitude estimation.

3.2.2. Navigation

3.2.2.1. QUEST Implementation

The QUEST implementation focuses on deriving the CubeSat's attitude using measurements from the onboard sensors through quaternion estimation. This process enables the computation of the Direction Cosine Matrix (DCM) and the angular velocity ω , to ensure accurate and reliable input for the control system.

The quaternion estimation process was implemented using the **q method** presented in Equation 3.2, which derives the quaternion based on measurements from the onboard sensors [4].

$$\hat{q} = \alpha \cdot \begin{pmatrix} \text{adj}(pI_3 - S)Z \\ \det(pI_3 - S) \end{pmatrix} \quad (3.2)$$

This method is based in Wahba's problem, which seeks to find the orthogonal matrix A with determinant $+1$ that minimizes the loss function presented in Equation 3.3. In this equation, b_i represents N unit vectors measured in the spacecraft's body-fixed frame, while r_i are the corresponding unit vectors expressed in the inertial reference frame. Each measurement is weighted by a non-negative scalar α_i , which accounts for the precision and reliability of the corresponding sensor.

$$L(A) = \frac{1}{2} \sum_{i=1}^N \alpha_i \|b_i - Ar_i\|^2 \quad (3.3)$$

To solve this optimization problem, the intermediate matrix B was constructed in Equation 3.4 using the measurements b_i , the reference directions r_i , and their associated weights α_i . The weighting factors α_i , assigned to each sensor measurement as $1/\sigma^2$, to account for their precision and reliability, were normalized, as shown in Equation 3.5.

$$B = \sum_{i=1}^n \alpha_i b_i r_i^T \quad (3.4) \quad \alpha_i^{\text{normalized}} = \frac{\alpha_i}{\sum_{j=1}^N \alpha_j} \quad (3.5)$$

From B , additional matrices and vectors necessary to construct the quaternion were derived. The vector Z , as shown in Equation 3.6, accounts for the cross products between the measured and reference vectors, while the symmetric matrix S was computed according to Equation 3.7. These matrices formed the foundation for calculating the parameter p , which represents the largest eigenvalue of B , and it was computed using its trace and the maximum eigenvalue, as shown in Equation 3.8.

$$Z \equiv \begin{bmatrix} B_{23} - B_{32} \\ B_{31} - B_{13} \\ B_{12} - B_{21} \end{bmatrix} = \sum_{i=1}^N \alpha_i (b_i \times r_i) \quad (3.6) \quad S = B + B^T \quad (3.7) \quad p = \lambda_{\max} + \text{tr}(B) \quad (3.8)$$

Considering $\lambda_{\max} = \{\alpha_1^2 + \alpha_2^2 + 2\alpha_1\alpha_2[(b_1 \cdot b_2)(r_1 \cdot r_2) + \|b_1 \times b_2\| \|r_1 \times r_2\|]\}^{1/2}$.

Using these elements, the quaternion \hat{q} was assembled, as described in Equation 3.2, and then normalized to remove the scaling factor α , yielding the optimal unit quaternion that best describes the CubeSat's orientation.

With the quaternion determined, the DCM was derived using the expression in Equation 3.9 to describes the transformation from the body frame to the inertial frame.

$$A = \begin{bmatrix} q_4^2 + q_1^2 - q_2^2 - q_3^2 & 2(q_1q_2 - q_4q_3) & 2(q_1q_3 + q_4q_2) \\ 2(q_1q_2 + q_4q_3) & q_4^2 - q_1^2 + q_2^2 - q_3^2 & 2(q_2q_3 - q_4q_1) \\ 2(q_1q_3 - q_4q_2) & 2(q_2q_3 + q_4q_1) & q_4^2 - q_1^2 - q_2^2 + q_3^2 \end{bmatrix} \quad (3.9)$$

Finally, the angular velocity ω was calculated by reversing the kinematic relationship expressed in Equation 3.10. By using the time derivative of the DCM and the skew-symmetric matrix ω^* , as described in Equation 3.11, the angular velocity vector was obtained.

$$\frac{dA}{dt} = -\omega^* A \quad (3.10) \quad \omega^* = \begin{bmatrix} 0 & -\omega_z & \omega_y \\ \omega_z & 0 & -\omega_x \\ -\omega_y & \omega_x & 0 \end{bmatrix} \quad (3.11)$$

3.2.2.2. State Observer

To refine the estimation of the spacecraft's angular velocity, a Linear State Observer was implemented to filter the initial angular velocity approximation. The observer design is based on a linearized model of Euler's equations, as shown in 2.2, around the equilibrium point $w_e = [0, 0, w_s]$ where w_s represents the angular velocity at which the CubeSat rotates about its principal \hat{z} axis. The system model is defined using the state-space representation matrices A, B, C, and D. Matrices A and B are derived by truncating the full system equations utilized in the Sun Pointing control section 3.2.3.1, which is covered in a subsequent part of this report. For the observer, C is modeled as a 3×3 identity matrix to reflect that angular velocity estimates can be directly obtained from system measurements, and D is set to zero. The observer state can now be expressed using linear relations as

$$\dot{\hat{x}} = (A - LC)\hat{x} + Bu + Ly \quad (3.12)$$

where u is the control action applied to the satellite (torque) while y is the estimation of ω retrieved by the kinematic inversion and L is a 3×3 matrix. The gain matrix L was designed using principles of optimal observation theory and refined through iterative tuning to ensure accurate performance. , and assumes the values of

$$L = \begin{bmatrix} 0.2113 & 0.0055 & 0 \\ 0.0055 & 0.2131 & 0 \\ 0 & 0 & 0.0258 \end{bmatrix} \quad (3.13)$$

By evaluating the observer equation 3.12 and integrating $\dot{\hat{x}}$, a filtered angular velocity ω is obtained. This refined angular velocity estimate is essential for enhancing the accuracy and stability of the CubeSat's navigation system. While the derivation of matrices A and B aligns with the Sun Pointing control design discussed later, their role here focuses exclusively on the observer's functionality, ensuring the precision of attitude estimation under dynamic conditions.

3.2.3. Control

The control subpart of the ADC Subsystem was designed to align with the mission objectives and is structured into three main components: a de-tumbling control law, which stabilizes the spacecraft after separation from the kicking stage; a linear Sun-pointing control law, utilized during nominal operations to ensure alignment with the Sun; and a globally stable Lyapunov-based re-pointing law, which guides the spacecraft back to its nominal operational configuration. The latter control law was developed by adapting the linear Sun-pointing law to satisfy the global stability conditions required by Lyapunov's Second Theorem.

3.2.3.1. Sun Pointing Law

The Sun-pointing control law for this spacecraft, inspired by the MOVE-II mission [8], is designed to maintain the $+\vec{Z}_b$ face aligned with the Sun, while ensuring the spacecraft spins around its \hat{z} axis at a constant angular rate, w_s , of 0.05 rad/s. This spin rate was selected to provide sufficient gyroscopic stiffness for stabilization while not interfering with active control maneuvers. Furthermore, this value is approximately 60 times the mean orbital angular velocity of the satellite, making it an optimal choice for the mission's operational requirements. The decision to implement a spinning spacecraft design was motivated by the need for robustness during eclipse phases, when full attitude determination may not be available. In such scenarios, passive stabilization ensures that small deviations from the desired Sun-pointing configuration are mitigated, even in the absence of active control interventions.

To approach the control problem a linearized system, in the form of $\delta\dot{x} = A\delta x + B\delta u$, was obtained by the dynamics of the system expressed in equation 2.1 and the kinematics of the sun direction vector in body frame \vec{s}^b :

$$\dot{\vec{s}}^b = -\vec{w}^b \wedge \vec{s}^b \quad (3.14)$$

By linearize around the equilibrium point $\vec{w} = [0; 0; \omega_s]$ and $\vec{s} = [0; 0; 1]$ and removing the rows and columns relative to the state variable s_z we obtain:

$$A = \begin{bmatrix} 0 & w_s & 0 & -1 & 0 \\ -w_s & 0 & 1 & 0 & 0 \\ 0 & 0 & 0 & \frac{I_y - I_z}{I_x} w_s & 0 \\ 0 & 0 & \frac{I_z - I_x}{I_y} w_s & 0 & 0 \\ 0 & 0 & 0 & 0 & 0 \end{bmatrix} \quad B = \begin{bmatrix} 0 & 0 & 0 \\ 0 & 0 & 0 \\ \frac{1}{I_x} & 0 & 0 \\ 0 & \frac{1}{I_y} & 0 \\ 0 & 0 & \frac{1}{I_z} \end{bmatrix} \quad \delta x = \begin{bmatrix} s_x \\ s_y \\ w_x \\ w_y \\ w_z - w_s \end{bmatrix}$$

The linear control problem was addressed using Optimal Control Theory by designing the weight matrices Q and R. The process started with an initial estimation of the weights, obtained by setting maximum allowable values for the states and control inputs, this was achieved by prioritizing a control strategy based on the vector \vec{s} , which can be directly measured with high precision, rather than relying on the indirect measurement of the angular velocity vector $\vec{\omega}$. The weight matrix R was specifically configured to ensure that the control inputs remain within the operational limits of the spacecraft's actuators and do not compromise the structural integrity of the spacecraft. After iterative tuning, the

final weight matrices were defined as Equation 3.15.

$$Q = \text{diag}\left(\frac{1}{(3e-1)^2}, \frac{1}{(3e-1)^2}, \frac{1}{(6e-1)^2}, \frac{1}{(6e-1)^2}, \frac{1}{(4e-3)^2}\right) * 1.115 \quad (3.15)$$

$$R = \text{diag}\left(\frac{1}{(9e-3)^2}, \frac{1}{(9e-3)^2}, \frac{1}{(9e-3)^2}\right) * 7e-1 \quad (3.16)$$

The Riccati equation was solved to determine the following gain matrix associated with the control law $\underline{u} = -K\underline{\delta x}$

$$K = \begin{bmatrix} -0.0023 & 0.0378 & 0.0602 & 1.1905e-4 & 0 \\ -0.0378 & -0.0036 & 5.4184e-5 & 0.0867 & 0 \\ 0 & 0 & 0 & 0 & 2.8397 \end{bmatrix} \quad (3.17)$$

3.2.3.2. Re-Pointing / Slew Maneuver Law

The sun pointing law designed, as detailed in section 3.2.3.1, is guaranteed to be stable only in states close enough to the equilibrium one. To extend its stability to the whole state space, Lyapunov second theorem was used to adequately modify the gain matrix K. Defining $\vec{\omega}_e = \vec{\omega} - \vec{\omega}_s$, $\Gamma = \vec{s}^b$ and $\Gamma_D = [0; 0; 1]$ is easy to prove that the Lyapunov candidate function 3.18 coupled with the control function 3.19 constitute a globally asymptotically stable system.

$$V(x) = \frac{1}{2} \langle \vec{\omega}, I\vec{\omega} \rangle + k_2(1 - \Gamma_D^T \Gamma) \quad (3.18)$$

$$\underline{u} = -k_1 \vec{\omega}_e - k_2 \Gamma_2 + k_2 \Gamma_1 \quad (3.19)$$

By choosing $k_2 = 0.0378$ and letting k_1 a generic diagonal positive semi-defined 3x3 matrix, we can express 3.19 as $\underline{u} = -K_l \underline{\delta x}$, where K_l is a matrix obtained by suppressing some selected terms from the SunPoiting gain matrix 3.17:

$$K_l = \begin{bmatrix} 0 & 0.0378 & 0.0602 & 0 & 0 \\ -0.0378 & 0 & 0 & 0.0867 & 0 \\ 0 & 0 & 0 & 0 & 2.8397 \end{bmatrix}$$

This enable us to just use K_l as control law for both the Sun poiting Phase and the slew manouver one.

3.2.3.3. Detumbling

For de-tumbling, a simple control logic, proportional to $\underline{\omega}^b$, was used. This control law takes the form of $\underline{u} = -K_{\text{det}} \underline{\omega}^b$, where K_{det} is the following matrix:

$$K_{\text{det}} = \begin{bmatrix} 0.0272 & 0 & 0 \\ 0 & 0.0272 & 0 \\ 0 & 0 & 0.0272 \end{bmatrix}$$

The values of this matrix were obtained by tweaking them based on an iterative approach, checking how tweaking the values effected the overall close loop performance in the simulator. Is important to notice that for any positive definitive matrix K the control law described above is globally asymptotically stable.

4 | Results

To assess the overall performance of the control system, a simulation campaign was conducted in two phases. The first phase involved evaluating the system's behavior over a selected set of initial conditions to observe its performance after the transient period had been completed. The second phase consisted of a series of Monte Carlo simulations aimed at assessing the control system's performance during de-tumbling and slew maneuvers. The results are presented in this chapter.

4.1. Control Results

An initial analysis of the control performance was conducted by simulating two orbits. The analysis began by evaluating the Attitude Pointing Error (APE), computed as $\arccos(\vec{Z}_b \cdot \vec{S}_b)$ since the mission objective is to point along the \hat{Z}_b axis. The initial conditions included an APE of nearly 90° and an initial angular velocity corresponding to a situation immediately after de-tumbling, with $\omega_i = [0, 0, 1e^{-4}]$. Due to the chosen orbit, no eclipse occurred during the observed period.

As shown in Figure 4.1, the pointing error quickly converges (around $t \sim 20s$) to a value close to 0, remaining bounded by an absolute error of less than 1° throughout the entire duration, thus meeting the pointing requirement. The flickering observed in the error is due to a similar phenomenon occurring with the angular velocities, as can be seen in Figure 4.2.

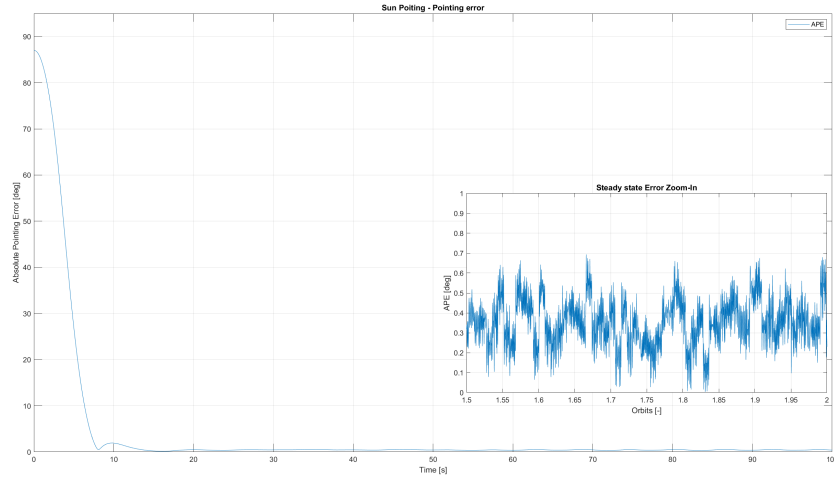


Figure 4.1: APE of satellite

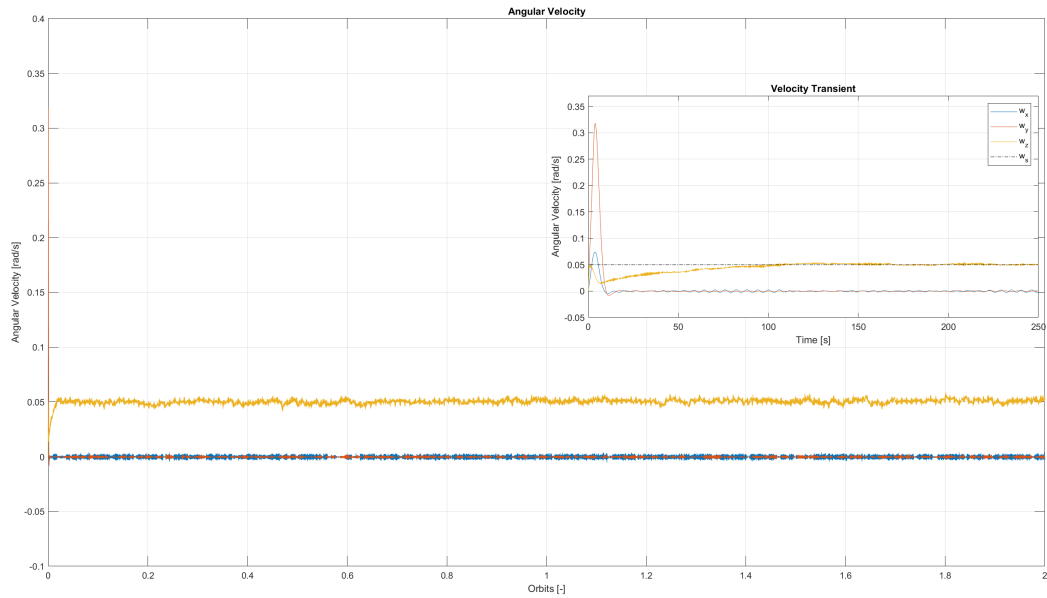


Figure 4.2: Angular Velocities During Pointing

By analyzing the angular velocities, it is possible to see how they are well behaved and bounded to their asymptotical desired values $\omega_d = [0, 0, \omega_s]$ after a fast transient of around 100s.

Here, it is also possible to observe the flickering effect mentioned before. This is due to two separate causes. The first one is the impossibility for the navigation subsystem to produce a perfect estimation of the angular velocity of the spacecraft, due to the noise present in the sensors. The second one is the error introduced by actuators hardware limits, that prevent it from producing arbitrary small correction torques.

4.2. Monte-Carlo test campaign

To complement the theoretical stability analysis and design reported in Chapter 4, and the preliminary performance analysis, a series of Monte-Carlo simulations were conducted to verify the asymptotic stability of the system and its performance.

4.2.1. Re-Pointing Monte-Carlo

First, a series of 175 test involving the Slew / Re-pointing law were conducted, where a random attitude has been selected between the space of all possible attitudes, and the system was let evolve for 1.5 orbits. As it can be observed in figure 4.3, all tested scenarios converge quickly (in under 100s) to the correct pointing direction, and the error stays in the neighborhood of 0 for the rest of the time, confirming experimentally what was demonstrated theoretically.

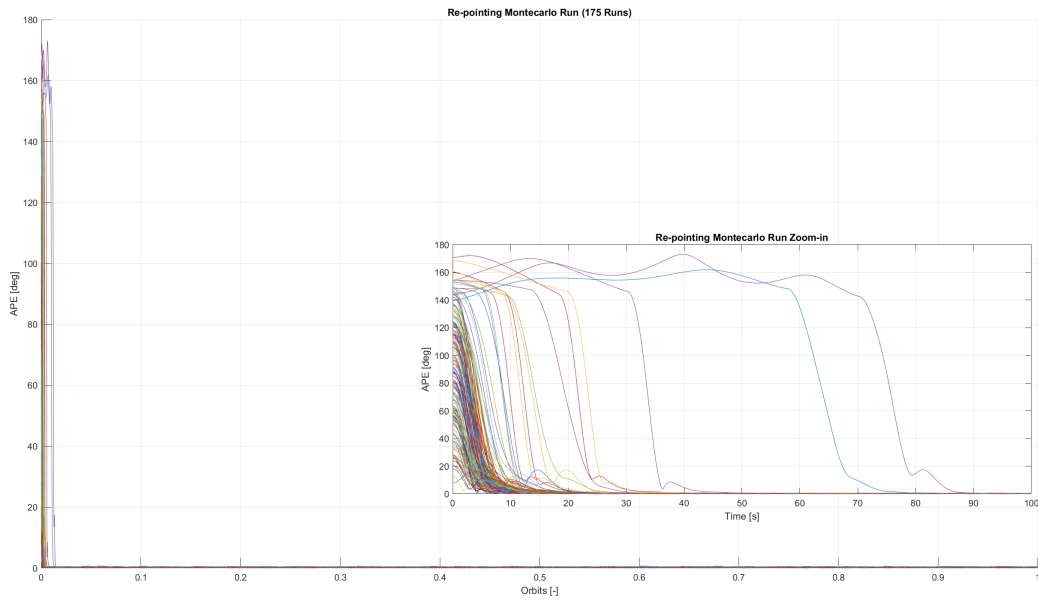


Figure 4.3: APE for a 175 samples Monte-Carlo analysis

4.2.2. De-tumbling Monte-Carlo

To validate the de-tumbling design, a Monte Carlo analysis was conducted over 300 samples, with each run differing based on its initial angular velocities. As shown in Figure 4.4 ω_x and ω_y converge to zero more quickly than ω_z . This is likely due to the difficulty of directly measuring the actual angular velocity of the spacecraft, requiring reliance on a state observer that is linearized around a non-zero angular velocity configuration.

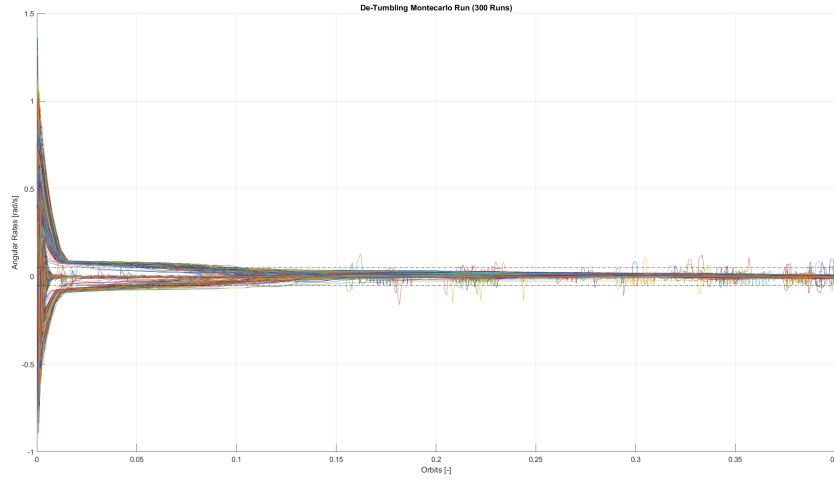


Figure 4.4: Angular Rates of the SpaceCraft during a 300 cases Montecarlo Analysis

Despite this, it is important to note that all angular velocities remain below 0.5 rad/s, in magnitude, shortly after 1/10th of an orbit. Additionally, while some angular velocity peaks are observed after convergence, these peaks are effectively handled by the control system, preventing significant issues.

4.3. Eclipse behavior

Due to the employment of the Sun sensor as the main sensing device in this mission, it is impossible, without adding other sensors, to retrieve the attitude of the satellite while being in an eclipse. While the orbit designed, as detailed in Chapter 1, minimize the amount of time spent in eclipse, the chosen semi-major axis do not guarantee the absence of an eclipse period. The Cubesat OBC software was developed to stop active control during the eclipse phase and rely only on the stability provided by its spinning around the major inertial axis. That is because, during this mission phase pointing requirement lose meaning. Consequently, the main mission goal became to maintain the satellite in a stable condition, to preserve the satellite integrity and resume steadily operations as soon as the eclipse has ended. To confirm this behavior, a simulation spanning 1 orbit was conducted, with the control system being initially switched off, then activated at $\frac{T_{orb}}{8}$. The satellite then entered into the eclipse at $\frac{3T_{orb}}{8}$ until $\frac{7T_{orb}}{8}$.

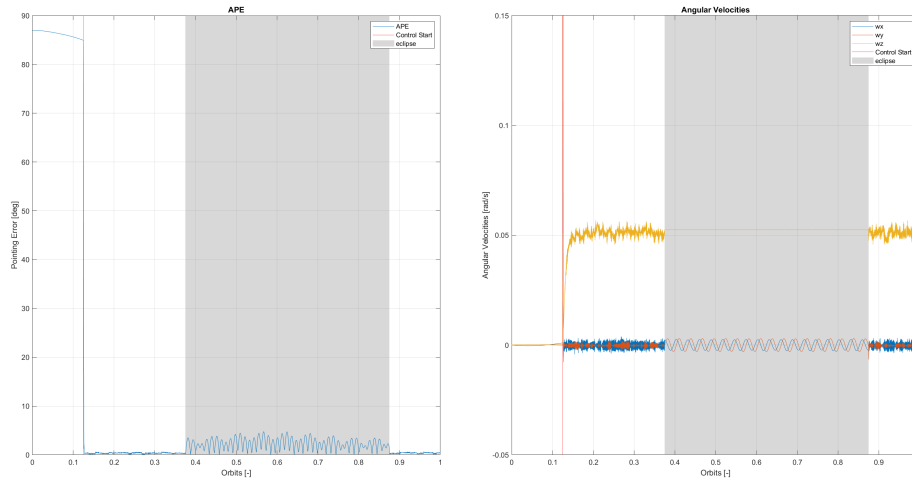


Figure 4.5: Behavior During Eclipse

As we can see in the picture, during eclipse the overall error remains bounded under 10° . It also converges quickly back to the near 0 value as soon as the control is switched back on, fulfilling the pointing requirements.

5 | Conclusions

As demonstrated by both the theoretical analysis and simulation results, the developed ADC subsystem is capable of pointing the sun outside the eclipse window, with a pointing error of less than 1° , as specified by the mission requirements. Future work should focus on enhancing the actuator's control logic to address issues arising from its inability to generate arbitrarily small reaction torques. Additionally, the overall navigation algorithm could be improved to reduce the AKE, potentially by incorporating an additional gyroscope. Finally, since the current model cannot perform detumbling during eclipses, a navigation algorithm based on Equation 3.14, along with a state observer, could be developed to enable detumbling capabilities using only magnetic field measurements.

Bibliography

- [1] NanoAvionics, *6u cubesat nanosatellite m6p*, <https://nanoavionics.com/small-satellite-buses/6u-cubesat-nanosatellite-m6p/>, Accessed: 2023-12-04, 2023.
- [2] M. E. Grøtte, R. Birkeland, E. Honoré-Livemore, *et al.*, “Ocean color hyperspectral remote sensing with high resolution and low latency—the hypso-1 cubesat mission,” *IEEE Transactions on Geoscience and Remote Sensing*, vol. 60, 2022.
- [3] I. Vertat and A. Vobornik, “Efficient and reliable solar panels for smallcubesat picosatellites,” *International Journal of Photoenergy*, vol. 60, 2014. DOI: 0.1155/2014/537645.
- [4] F. L. Markley and J. L. Crassidis, *Fundamentals of Spacecraft Attitude Determination and Control*. Springer, 2014.
- [5] NASA, “Spacecraft magnetic torques,” NASA, Tech. Rep., 1969.
- [6] SolarMems, *Nanossoc-d60 technical specification*, <https://www.cubesatshop.com/wp-content/uploads/2016/06/nanoSSOC-D60-Technical-Specifications.pdf>, Accessed: 2025-01-03.
- [7] N. Baker, “Feasibility and design of miniaturized control moment gyroscope for a 3-axis stabilized micro satellite,” Lulea University, Tech. Rep., 2016.
- [8] D. Messmann and all, “Magnetic attitude control for the move-ii mission,” *EUCASS*, 2017.